



Full Text View

[Volume 32, Issue 2 \(February 2002\)](#)

Journal of Physical Oceanography

Article: pp. 527–544 | [Abstract](#) | [PDF \(1017K\)](#)

Sampling Characteristics from Isobaric Floats in a Convective Eddy Field^{*}

Sonya Legg

Woods Hole Oceanographic Institution, Woods Hole, Massachusetts

James C. McWilliams

Institute for Geophysics and Planetary Physics, University of California, Los Angeles, Los Angeles, California

(Manuscript received May 19, 2000, in final form April 3, 2001)

DOI: 10.1175/1520-0485(2002)032<0527:SCFIFI>2.0.CO;2

ABSTRACT

During the recent Labrador Sea Deep Convection Experiment, numerous isobaric floats were deployed. Interpretation of the quasi-Lagrangian measurements from these floats requires an understanding of any biases that may be introduced by the response of the floats to the flow in which they are embedded. To investigate the float measurement biases in convecting flow numerical simulations of isobaric floats in a domain containing several mesoscale eddies have been performed. When a surface heat loss is applied, spatially variable convective mixing and baroclinic instability result. The authors find that without surface cooling, probability density functions of Eulerian and isobaric float measurements of tracers and velocities are very similar, given an initial distribution of isobaric floats that is random with respect to the initial features of the tracer field. However, with cooling isobaric statistics are biased compared to the Eulerian statistics. In particular, in near-surface regions isobaric floats appear to oversample regions of dense downwelling fluid. Since in near-surface layers downwelling dense fluid is associated with convergence, a probable explanation of the isobaric float biases is a tendency for floats to concentrate in regions of horizontal convergence. Also, with cooling floats may be more easily exchanged between eddies and the ambient fluid. The escape of a float from an eddy can be identified from changes in the values of material tracers. The authors identify a positive skewness in the time derivative of the buoyancy measured by the individual near-surface floats as a indicator of convection in the presence of mesoscale eddies.

Table of Contents:

- [Introduction](#)
- [Numerical model](#)
- [Results](#)
- [Conclusions](#)
- [REFERENCES](#)
- [FIGURES](#)

Options:

- [Create Reference](#)
- [Email this Article](#)
- [Add to MyArchive](#)
- [Search AMS Glossary](#)

Search CrossRef for:

- [Articles Citing This Article](#)

Search Google Scholar for:

- [Sonya Legg](#)
- [James C. McWilliams](#)

The recent Labrador Sea Deep Convection Experiment ([Lab Sea Group 1998](#)) employed a variety of observational techniques to examine wintertime deep convection in the Labrador Sea. These included traditional ship-based measurements in a few sections across the basin, Eulerian measurements from moored arrays, and Lagrangian or quasi-Lagrangian measurements by a variety of floats. Some floats were designed to follow the full three-dimensional motion of a water parcel as closely as possible ([D'Asaro et al. 1996](#)), while others were constrained to follow motion on a particular isobaric surface ([Lavender et al. 2002](#)). Analysis of the data from these floats requires an understanding of the biases that may be introduced into the measurements by the response of the floats to the flow in which they are embedded. In this article we describe the principal differences between Eulerian and isobaric float measurements of a numerically simulated actively convecting region. Previous studies have examined the response of fully three-dimensional floats and isobaric floats to small-scale convection plumes ([Harcourt et al. 1997, 2002](#); [Harcourt 1999](#); [Lherminier et al. 2001](#)) and the response of isobaric floats to the basin-scale currents in the Labrador Sea ([Lavender et al. 2001](#)). Here we examine the response of isobaric floats in a medium-scale domain, containing several mesoscale eddies and spatially variable convection. We have made extensive analysis of the dynamics of this regime in [Legg et al. \(1998\)](#), [Legg and McWilliams \(2000, 2001\)](#); hereafter LM2000 and LM2001, respectively). LM2000 in particular describes the eddy dynamics of these same simulations, so that we will only briefly summarize the dynamics here and concentrate instead on the sampling characteristics.

2. Numerical model

The numerical domain has dimensions $100 \text{ km} \times 100 \text{ km} \times 2 \text{ km}$, and initially contains 16 surface-intensified baroclinic eddies, both cyclonic (associated with denser cores and weaker stratification) and anticyclonic (lighter cores and stronger stratification). We carry out two companion numerical simulations over an interval of 37 days: in one the domain is cooled uniformly at the surface, while in the other there is no surface forcing. In both, 1600 floats are placed near the surface at a depth $h = -62.5 \text{ m}$, and another 1600 at a depth of -1062.5 m on a regularly spaced grid. The floats are thereafter allowed to drift in response to the flow, and the three velocity components and tracer values at the float locations are continuously recorded. The numerical floats are therefore most similar to the isobaric Profiling Autonomous Lagrangian Circulation Explorer (PALACE) floats of [Lavender et al. \(2002\)](#), which record vertical velocity, temperature, and salinity continuously as they move with the flow at a particular predetermined pressure level. However, whereas PALACE floats periodically move to the surface in order to transmit their data, profiling temperature and salinity with depth as they go, our floats remain at the predetermined depth over their entire lifetime.

The fluid dynamical numerical model is a three-dimensional nonhydrostatic model with an implicit gravity wave formulation (A. J. Adcroft 2000, unpublished manuscript), run with a horizontal resolution of $\Delta x = \Delta y = 390 \text{ m}$ and a vertical resolution of $\Delta z = 125 \text{ m}$ and a temporal resolution of $\Delta t = 35.7 \text{ s}$. Horizontal slices of all fields at the particular vertical levels we have chosen for the float calculations were saved every five time steps. The float calculation was then run offline. The float model uses a fourth-order Runge–Kutta time-stepping scheme, and spectral splines for interpolating fields in the horizontal to the float position. The float model time step is equal to five of the fluid dynamical model time steps, and interim values of fields for the interim Runge–Kutta time derivatives are obtained by linear interpolation in time. This difference between the float model and fluid dynamical model time steps is possible because the floats move only in two dimensions, while the fluid moves in three dimensions. The fluid dynamical model time step is chosen to satisfy the Courant–Friedrichs–Lewy (CFL) criterion $\Delta t \leq \epsilon \Delta z / W$, where Δz is the vertical resolution and W is the maximum vertical velocity. Since the fluid dynamical model uses an Adams–Bashforth time-stepping scheme, stability considerations require that $\epsilon < 1$, with a typical limit being about $\epsilon \leq 0.2$. By contrast, the float model need only satisfy the CFL criterion with respect to horizontal motion: $\Delta t \leq \epsilon \Delta x / U$, where Δx is the horizontal resolution and U is the maximum horizontal velocity. For convecting motion $U \approx W$. Then, since $\Delta x = 3.125 \Delta z$, a larger time step is possible for the float model. Furthermore, the robust Runge–Kutta time-stepping scheme used in the float model means that ϵ may be larger than for the fluid dynamical model. Hence a float time step equal to five fluid dynamical time steps is consistent with considerations of numerical stability. Of course, small errors are introduced by increasing the time step, but these have to be balanced against the practical difficulties of saving large data volumes from the fluid dynamical model at every time step. We tested the accuracy of the time-stepping scheme by integrating the float model for 12 days using a frozen nondivergent horizontal velocity field, identical to that used to initialize the fluid dynamical model. The floats follow the streamlines very closely and maintain closed paths around the eddies to within 2% of the path radius per rotation time. There is no discernible bias between the trajectories around cyclonic eddies and anticyclonic eddies. In both cases trajectories that tend to gradually spiral inward and outward were found with equal frequency.

Instead of temperature and salinity, we show results for buoyancy, $b = g(\alpha T - \beta S)$, and spice, $\tau = g(\alpha T + \beta S)$. Buoyancy is the active tracer, which influences the dynamics, whereas spice is purely passive. The differences in the variability of buoyancy and spice are studied in LM2000. The initial conditions, described in more detail in LM2001 consist of a stable background buoyancy stratification, into which dense-core and light-core eddies are embedded. The background τ stratification consists of low τ fluid above high τ fluid (which when combined with the buoyancy stratification decomposes into cold fresh fluid above warm salty fluid), while the dense eddies are associated with salty fluid (higher τ), and light-core eddies are associated with fresher fluid (lower τ). The surface forcing consists of equal buoyancy loss and τ loss, corresponding to cooling without any salt flux.

3. Results

a. Overview of the eddy evolution

A complete description of the eddy evolution is given in LM2001. However, for the reader's convenience we summarize the pertinent results here. [Figure 1](#) shows snapshots of the near surface buoyancy and τ at the start of the calculation and on the 12th and 37th days of cooling. [Figure 2](#) shows the vertical velocity on the 12th and 37th days of cooling. The float positions are shown by superimposed black crosses; four larger colored crosses indicate floats discussed in more detail later. Initially there are several cyclonic dense, high τ (salty) eddies, and several anticyclonic, light eddies. The eddies are initially stable to baroclinic instability, being of the order of the deformation radius in size. Following the erosion of stratification by the surface buoyancy loss and consequent reduction in L_ρ , they become unstable. After 12 days the dense eddies have all shed lobes and partially broken up through instability. At this time there is little plume-scale activity visible, and most of the mixing is in the form of slantwise convection associated with the baroclinic instability. There is a tendency for floats to congregate both within the dense eddies and along the fronts separating light and dense fluid. These fronts are associated with downwelling. The organization of downwelling by the eddy field into long thin fronts is evidence for slantwise, as opposed to plume-scale, convection. The horizontal separation between downwelling regions in this type of convection regime is typically much greater than the depth of the convectively modified layer (<1 km at this time). The regions of lightest fluid now contain very few floats. Later the convectively mixed region reaches throughout the domain, and horizontal buoyancy differences have largely been eroded. Then plume convection takes over and cellular convection patterns are visible in the density field at 37 days. Now the horizontal scale of the downwelling regions is of the order of the convection layer depth ≈ 1.8 km. However, some fragments of the original eddies remain in both buoyancy and τ fields, still associated with cyclonic vorticity. At this time the velocity field is dominated by an energetic barotropic horizontal eddy field, in contrast to the initial baroclinic velocity field. (See LM2001 for further details.)

The horizontally averaged buoyancy as a function of depth and time ([Fig. 3](#)) shows the deepening of the convectively modified layer with time. The isopycnals are progressively modified from the surface down. Initially, the convectively modified layer is not actually “mixed” since a slight positive buoyancy gradient persists. This is a consequence of the horizontal eddy structure, with slantwise convection predominating and isopycnals sloping rather than vertical. With time, the erosion of the horizontal buoyancy anomalies allows vertical plume convection to take over, and isopycnals become more vertical in the convectively modified layer from about 20 days onward. However, the convective layer depth is highly spatially variable, especially during the first half of the integration when horizontal buoyancy differences are large, so this horizontal average gives an incomplete description of the behavior of the convectively modified layer.

b. PDFs


[Figure 4](#) shows the probability distribution functions (PDFs) for buoyancy (b), spice (τ), and the vertical component of velocity (W), from both the Eulerian grid and the isobaric floats, at the beginning of the calculation when floats are initialized and cooling begins (Init) and at the end of the calculation on the 37th day of surface cooling (Cool). For comparison, results at the end of the same time period but without any cooling are also shown (Control). The PDFs are shown both near the top surface and at middepth. All the statistical quantities (mean, rms, skewness) described later derive from the PDFs. The PDFs are normalized so that $\int_{-\infty}^{\infty} \text{PDF}(x) dx = 1$. Initially the Eulerian and isobaric float measurement PDFs are almost identical (Init), as would be expected, the differences being due to the smaller number of floats (1600) as compared to Eulerian grid points (65 536). In fact, to obtain smooth PDFs from the isobaric float measurements, data from 10 consecutive time steps were combined, giving a total of 16 000 measurements in the sample, but still considerably less than the Eulerian measurements. At the end of the calculation without cooling (Control), both Eulerian and isobaric float PDFs have been significantly modified due to the eddy-interaction processes that have taken place. However, the differences between the Eulerian and isobaric float PDFs are small. In contrast, there are significant differences between the isobaric float and Eulerian PDFs in the simulation with cooling (Cool). Both isobaric float and Eulerian PDFs are shifted to lower buoyancy (reflecting the surface buoyancy loss) and higher τ (reflecting the mixing of higher τ fluid from below, despite the surface τ loss). However, despite this broad similarity, there is a double peak in the isobaric float buoyancy and spice PDFs near the top surface. The secondary peak, on the low-buoyancy flank of the Cool float b PDF, and on the high τ flank of the Cool float τ PDF, corresponds to denser and saltier than average fluid and suggests a tendency for the isobaric floats near the surface to congregate in salty dense regions. From [Fig. 1](#) we can see that dense, high τ regions continue to be associated with remnants of the original dense-core eddies, although there is with time also higher τ in upwelling regions associated with convection cells. [Figure 1](#) shows that floats do tend to congregate in the remnants of the original dense core eddies, as suggested by the double peaks of the PDFs. The vertical velocity PDF has broadened considerably following cooling, reflecting the presence of active convection, but the peak in the isobaric float PDF is at more negative (downward) velocities than the Eulerian PDF.

At middepth, on the 37th day of cooling (by which time convection extends well below middepth) the differences between Eulerian and isobaric float PDFs are not as marked as in the surface layers, but there is again a tendency for more floats in denser, colder regions.

Horizontal velocity PDFs are not shown since there is no significant difference between the isobaric float and Eulerian PDFs for these fields. Both convergent and divergent regions are associated with minima in horizontal velocity magnitude. Hence, a tendency for floats to congregate in convergent regions and leave divergent regions would have no net effect on the horizontal velocity PDFs.

These PDFs indicate that with the addition of cooling, the response of isobaric floats to the flow is significantly different than without cooling (when there is little difference between Eulerian and isobaric float PDFs, even when considerable flow evolution has taken place). We now focus on the time evolution of the differences between Eulerian and isobaric float statistics in the convective eddy scenario.

c. Comparison between isobaric float and Eulerian time series


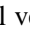
[Figure 5](#)  shows the time series of the mean buoyancy, spice, and three velocity components near the top surface, as measured by the Eulerian grid (solid) and the floats (dashed). The mean is defined as the average over all grid points on the horizontal plane in the Eulerian case and as the average over all floats in the horizontal plane in the isobaric float case.

The Eulerian horizontal mean of the horizontal velocities is close to zero, while the mean of the isobaric float measurements fluctuates due to the nonuniform spacing of the points. The amplitude of the fluctuations gives an indication of the error in the float measurements attributable to the finite number of measurements. For both horizontal velocity components, the difference between the isobaric float and Eulerian mean velocities is therefore of the order of magnitude of this error, without any statistically significant bias. By contrast the fluctuations in the isobaric float mean velocity are much smaller than the difference between the isobaric float and Eulerian mean vertical velocity. This difference therefore represents a significant bias. The isobaric float mean is biased toward downwelling, with the bias increasing with time. At this depth the association between convergence and downwelling can be seen by examining γW_{rms} , as in [Lherminier et al. \(2001\)](#), where γ is the Eulerian correlation between vertical velocity and convergence dW/dz :

$$\gamma = \frac{\langle W dW/dz \rangle}{W_{\text{rms}} dW/dz_{\text{rms}}}, \quad (1)$$


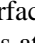
where angle brackets represent the horizontal average over the whole Eulerian grid, and γ is negative throughout the calculation. That the isobaric mean W closely follows the Eulerian γW_{rms} indicates that the convergence of floats in downwelling regions is a good explanation for the bias in the isobaric float measurement of W_{mean} .

The mean buoyancy (b) measured by the floats tends to become less than the Eulerian value, reflecting the presence of the second peak in the buoyancy PDF, due to the clustering of floats within convergence zones, associated with lower buoyancy. These dense regions, being fragments of the original dense, spicy eddies, are associated with greater spice than the surroundings, reflected in the higher mean spice measured by the floats as compared to the Eulerian grid. The differences between isobaric float and Eulerian means in buoyancy and spice may be small compared to the overall trends in the two, but they are significant compared to the sampling error suggested by the very small fluctuations in buoyancy and spice isobaric means. Note that the temperature $\alpha T = 0.5(b + \tau)$ is increasing near the surface, despite the surface cooling. This reflects the initial stratification in which colder water overlies warmer water. Mixing brings warmer water up from below, so warming the surface layers.

[Figure 6](#)  shows this comparison between Eulerian- and isobaric-mean quantities at middepth. Here, as indicated by the rms vertical velocity ([Fig. 7](#) ), convection only penetrates after about 20 days. Until that time the isobaric-mean buoyancy decreases compared to the Eulerian value, while the mean spice increases. Both Eulerian- and isobaric-mean buoyancy increase due to diffusion from the surface, while mean τ decreases, again due to diffusion from the surface. (This diffusion from the surface is an unavoidable consequence of the nonlinear gradients in initial buoyancy and τ fields, as well as the relatively large value of model vertical diffusivity. Identical vertical diffusion is found in the control case, which has the same gradients and diffusivity.) During this time period, there is a small bias toward downwelling (of about -0.05 mm s^{-1}). By contrast, in the control case (not shown) there is no systematic bias in the isobaric measurements of mean W . The bias in the convecting scenario may be associated with convectively initiated baroclinic instability. If the fluid is undergoing a baroclinic instability, we would expect denser regions to be slumping (i.e., downwelling). Hence the oversampling of downwelling regions would be associated with an oversampling of denser regions, as initially observed. Since the initial conditions associate dense-core eddies with higher τ , an increase in τ would also be associated with the oversampling of downwelling dense regions. Hence, we can explain the initial trends in the tracer fields by a tendency for floats to congregate in downwelling regions. We hypothesize that the downwelling is associated with baroclinic instability of the initial eddy field initiated by the surface convection.

After the convective layer deepens to 1 km, the differences between the isobaric float and Eulerian tracer measurements

diminish. Convergent zones at this level would be associated with vertically driven upwelling, giving rise to the upward bias in the isobaric float mean of vertical velocity. This conclusion is supported by the plot of Eulerian γW_{rms} , which is positive at this depth. Note that, whereas near the surface $\langle W \rangle \approx (2/3)\gamma W_{\text{rms}}$, at middepths $\langle W \rangle$ is only $\approx (1/3)\gamma W_{\text{rms}}$, implying a less straightforward relationship between convergence and eddy biases, perhaps due to the more complicated time history at this depth, which is initially below the convective layer. Upwelling regions would be associated with buoyant fluid and, if located in the light, fresh eddies, with lower spice values, hence reversing the isobaric float trend prior to convection. The trend in the bias in isobaric float measurements at middepth therefore varies with time, depending on the extent of the convectively active layer, unlike the bias near the surface. Here there is net cooling with time, as convection brings colder water down from the surface.

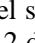
[Figure 7](#)  shows the isobaric float and Eulerian root-mean-square (rms) of b , τ , and W near the top surface and at middepth. The rms of a sample is defined as $\sigma = [(1/n) \sum_n (X_i - \bar{X})^2]^{1/2}$, where \bar{X} is the sample mean and n the number of realizations in the sample. The horizontal velocity rms time series are not shown since they are very similar for the Eulerian and isobaric float measurements, as are all higher moments of the horizontal velocities. Both near the surface and at middepth, the isobaric float measurements overestimate the rms in the buoyancy and spice fields and underestimate the rms of vertical velocity. The W rms is underestimated by the floats because floats have a bias toward remaining in convergent regions (as indicated by the mean), so only a fraction of the W distribution is sampled. The larger isobaric rms for b and τ near the surface reflect the broader isobaric distributions seen in [Fig. 4](#) , as well as the double peak seen in these distributions at late times.


In interpretation of field data, it is often impossible to obtain meaningful statistics by taking an ensemble average since the number of floats is too small. Instead, the anomaly of a quantity Q is calculated in each individual timeseries as

$$Q'_i = Q_i - \bar{Q}_i \quad (2)$$

where \bar{Q}_i is the low frequency component of time series Q_i . Then an estimate of the variance can be obtained from

$$\sigma^2 = \frac{1}{n} \sum_{i=1,n} (Q'_i)^2. \quad (3)$$

Here, for comparison, we use this method to calculate the buoyancy variance and velocity variance estimates for the near-surface level shown in [Fig. 8](#) . To obtain our low-frequency time series we conduct running averages over a window of 3.3 days, 8.2 days, and (for buoyancy only) 16.4 and 24.6 days. Note that this method only identifies the variance that occurs in the time series on timescales less than the averaging period. There is little difference between the new estimates of vertical velocity variance and the previous estimate using the float ensemble averages. This indicates that the ensemble variance in vertical velocity measurements is reproduced in the temporal variance in each time series on timescales < 3.3 days. However the buoyancy variance estimated by temporal averaging is much less than the previous estimate made using ensemble averages when the averaging timescale is 3.3 days. As the averaging timescale increases, the buoyancy variance estimate increases, but even for an averaging timescale of 16.4 days the variance is considerably smaller than that estimated by subtracting the ensemble mean. Hence, floats do not sample the full tracer variability present in the mesoscale eddy field over these time periods. Furthermore, much of the increase in variance at the beginning of the time series as the averaging timescale is increased can be ascribed to the nonlinearity of the background temperature trend—the 24.6 day temporal average buoyancy at time 12.3 days is always higher than the actual buoyancy because of the very high values of buoyancy in the early part of the time series. This suggests that it may be difficult to obtain a good estimate of the tracer variability from a small number of floats in a region where mesoscale eddies are the principal source of that variability, unless the time series are sufficiently long. (We also evaluated alternative methods of obtaining the low frequency components such as using more sophisticated filters and fitting a linear trend. Since the buoyancy time series are highly nonlinear, with an especially steep decline at early times, the linear fit produced a spurious W-shaped variance curve, while filtering produced similar results to the running averages over the central period of time.) The difference in behavior between the buoyancy variability and the vertical velocity variability sampled by the floats is a reflection of the Eulerian spectra of these fields. The vertical velocity spectrum is peaked at high frequency, while by contrast the buoyancy spectrum is distributed over a broader range of frequencies.

[Figure 9](#)  shows the isobaric and Eulerian skewness of b , τ , and W near the top surface and at middepth, where the skewness is defined as $S = (1/n) \sum_n (X_i - \bar{X})^3 / \sigma^3$. Near the surface, the isobaric float and Eulerian measurements agree for the vertical velocity field. The isobaric float measurements show an increased negative b skewness and an increased positive τ skewness, reflecting the low b and high τ secondary peaks in the PDFs at late times.

At middepth the vertical velocity field shows a negative skewness in the Eulerian measurements at the time when

convective downwelling first penetrates to this region. It is well known that in convective boundary layers driven by a flux from one surface, the vertical velocity is skewed in the direction away from the surface forcing, and this skewness increases with distance from that surface (Moeng and Wyngaard 1988). This is not reflected in the isobaric float measurements because the downwelling is associated with divergence at this level and therefore is not well sampled by the floats. The isobaric b and τ skewness initially closely follow the Eulerian measurements, but after convection reaches this level, a negative b skewness and positive τ skewness bias develop, as near the surface.

d. Float dispersion

Figure 10 shows the dispersion of the floats as a function of time, at middepth and surface, both with and without surface cooling. The dispersion is defined as

$$D(t) = \langle (x_i(t) - x_i(t_0) - M_x(t))^2 + (y_i(t) - y_i(t_0) - M_y(t))^2 \rangle, \quad (4)$$

where M_x and M_y are the mean zonal and meridional particle displacements:

$$\begin{aligned} M_x(t) &= \langle x_i(t) - x_i(t_0) \rangle; \\ M_y(t) &= \langle y_i(t) - y_i(t_0) \rangle, \end{aligned} \quad (5)$$

and angle brackets represent the mean over all particles. Figure 10 shows that over long times the dispersion is more or less linear with time, as would be expected for a diffusive process (Taylor 1921). This feature is unchanged by the addition of surface cooling and the associated divergence and convergence. Initially the dispersion increased like t^2 , but this period is short-lived. From the portion of the curve where $D(t) \sim t$ we can estimate a diffusivity D , which is given by

$$D = 4\kappa t \quad (6)$$

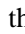
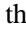
for a two-dimensional process (Chandrasekar 1943). This gives values of diffusivity as follows: near the top surface, $\kappa = 890 \text{ m}^2 \text{ s}^{-1}$ with cooling and $\kappa = 1140 \text{ m}^2 \text{ s}^{-1}$ without cooling; at middepth, $\kappa = 788 \text{ m}^2 \text{ s}^{-1}$ with cooling and $\kappa = 1100 \text{ m}^2 \text{ s}^{-1}$ without cooling. [Typical values of diffusivity observed from float measurements of mesoscale eddies are $O(10^3) \text{ m}^2 \text{ s}^{-1}$ (McWilliams et al. 1983)]. Given the rms horizontal velocity with cooling (not shown), which is approximately constant over the course of the cooling integration, this gives a mixing-length estimate $L = \kappa/V \approx 7.5 \text{ km}$. In the calculation without cooling, the rms horizontal velocity is continuously decreasing. If κ is constant in time, as indicated by the linear relationship between D and t , this implies an increasing mixing length L , perhaps associated with the enlargement of eddies through merger. The slightly smaller κ with cooling compared to without cooling may reflect the different character of the mesoscale eddy field with and without cooling.

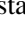

e. Trapping of floats in light and dense eddies


Figure 11 shows the mean b , τ , and W measured by floats initially in the densest and lightest regions of the flow in the surface layer, both with and without surface cooling. Initially all floats show a reduction in both b and τ due to the surface forcing. At the onset of convection, this reduction is briefly suppressed as lighter, warm, salty fluid is mixed up from below. The dense eddy floats show a brief rise in b and τ , while the light eddy floats show a rise in τ but only a slight reduction in the rate of decrease of b , perhaps because the change in density with depth is greater in the light eddies, so that fluid mixed up by convection is as dense as the surface cooled fluid. The onset of convection occurs earlier in the dense eddies (at about 3 days) and later in the light eddies (at about 5 days) since the dense eddies initially have weaker stratification and, hence less stability. As time proceeds the differences between fields measured by the two groups of floats diminish. This diminishing gap between the mean tracer values measured by the two groups of floats may be due to two different causes—an overall decline in the Eulerian variance in the tracer fields (Fig. 7) or a tendency for floats to escape from the eddies where they were initialized. To clarify the cause of the reduction in differences between light and dense eddy floats, Fig. 12 shows the buoyancy difference between the light eddy floats and the dense eddy floats scaled by the Eulerian buoyancy variance, $\Delta b/b_{\text{rms}}$, for both the cooling and control scenarios. With cooling, this ratio decreases throughout the calculation so that the final difference between the buoyancy measured by the initially light and dense eddy floats is less than the Eulerian rms value and of the order of the sampling error, so that floats have essentially been completely mixed up. With cooling we can fit this curve to an exponential decay of the form

$$\frac{\Delta b}{b_{\text{rms}}} = \left(\frac{\Delta b}{b_{\text{rms}}} \right)_{t=0} \exp\left(-\frac{t}{t_d}\right), \quad (7)$$

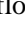
where $t_d = 15.8$ days. By contrast, without cooling, the ratio only declines slightly so that the mixing of floats between light and dense regions is not nearly as marked as in the convective scenario. This probably reflects the increased coherence of the eddies without cooling, with eddy destruction occurring only through the shedding of filaments during merger. With cooling eddies fragment through baroclinic instability, which may encourage the mixing of floats between initially different regions.

Evidence for float exchange between eddies and the ambient fluid can also be found in the individual float records. [Figure 13](#)  shows the tracks and buoyancy and spice time series from four individual floats in the surface layer, all of which were initially in or near the core of the same dense eddy. [Figure 1](#)  shows the locations of these four floats at the beginning of the calculation and on the 12th and 37th days of cooling, superimposed on the buoyancy and τ fields. Initially, before convection begins, all the floats show the same rate of decrease in buoyancy and τ , due to the surface cooling. At the onset of convection, at around 3 days, both b and τ increase suddenly in all floats as fluid is mixed up from below. Soon afterwards the floats show large oscillations in the values of b and τ , when the floats are affected by the large tracer gradients at the edges of the eddy, where the convergent zones are located. Large changes in tracer quantities measured by the floats can be induced by sudden mixing and engulfment of fluid with different properties, a process that likely occurs in these zones around the eddies, or when a float remains at the surface while the parcel it has been tracking is subducted and is replaced by a parcel with different properties, a process that occurs in the convergence zones.

In [Fig. 13](#) , the first float to leave the eddy is that shown in green: at about 7 days it is swept away from the eddy and remains in a parcel of relatively buoyant, relatively low τ fluid (in [Fig. 1](#)  it is the only float to have been detrained from the original eddy structure at $t = 12$ days). It is soon entrained into another cyclonic eddy, in which the buoyancy decreases faster and τ increases faster than average.

Other floats show similar features when they leave the original cyclonic eddy at times of 18 days (magenta) and 23 days (red): a sudden increase in buoyancy and decrease in τ , followed by a period with less oscillation in these quantities than when the floats were within the eddy. The float shown in blue appears to remain within a fragment of the original eddy throughout, without any transition to a higher buoyancy, lower τ state. For much of the latter half of the calculation this float records denser, higher τ fluid than the other floats. The final image in [Fig. 1](#)  shows that two floats are in or close to dense eddy structures (the blue and green floats) and two have been mixed into the surrounding fluid (the red and magenta floats).

f. Baroclinic eddy signatures in float time series

As described earlier, during the earlier part of the convecting period, the mixing is dominated by slantwise convection associated with the baroclinic eddies, while later, when horizontal buoyancy anomalies have been eroded, vertical plume convection takes over. While the resolution of our model is not sufficiently fine to examine the plume processes in detail, we can examine the baroclinic instability signatures in the float tracks. Those floats that originated in the dense eddies are particularly likely to be subjected to baroclinic instability since the fluxes are located predominantly at the edges of the dense eddies. [Figure 14](#)  shows time series of buoyancy anomaly and vertical velocity over the time period when baroclinic instability dominates. A common feature of these time series are sudden increases in buoyancy, which often follow a downwelling spike. Examples of such buoyancy jumps are seen at 8 days in the top left panel, 7.5 days in the top right panel, 6.5 and 9 days in the bottom left panel, and 6 and 9.5 days in the bottom right panel. By contrast, decreases in buoyancy are more gradual (and this is also true for those floats in light eddies). We hypothesize that the fluid tracked by the float becomes dense gradually due to the surface buoyancy forcing, and then the float measures a sudden increase in buoyancy when it is left near the surface, while the dense parcel it was formerly tracking is subducted in the downwelling front.

The tendency for buoyancy increases to be sudden, with more gradual decreases, can be quantified by examining the skewness of the buoyancy time derivative:

$$S = \frac{\frac{1}{n} \sum_n \left(\frac{db}{dt_i} - \overline{\frac{db}{dt}} \right)^3}{\sigma^3}, \quad (8)$$

where db/dt_i is the time derivative of the buoyancy time series measured by an individual float, $\overline{db/dt}$ is the ensemble mean

time derivative at a particular instant, and σ is the rms of the time derivative. Figure 15 shows the skewness of both the buoyancy and the vertical velocity time series. The skewness of db/dt is positive, indicating more sudden increases in buoyancy and gradual decreases, as deduced earlier from qualitative inspection of the individual time series. The skewness of dW/dt is smaller in magnitude and negative—the asymmetry is not so pronounced and is in the opposite direction with more sudden downwelling, a feature that we were not able to identify by visual inspection of our sample time series. The skewness of db/dt decreases with time as the baroclinic instability is replaced by more upright convection when horizontal buoyancy anomalies are eroded.

Open ocean measurements of a convective region by isobaric floats made by Lavender et al. (2002) indicated a similar difference between velocity and temperature time series to that described here, with velocity time series characterized by symmetric spikes and temperature by more steplike features identified qualitatively in the time series. However, the steps that Lavender et al. identify in the observed temperature time series include both sudden warming and sudden cooling. Also, since the salinity is not known in the observations, some of these changes may be density compensated and have no buoyancy signal. The few time series given in Harcourt (1999) for isobaric floats in horizontally homogeneous convection do not seem to show any steplike features in the buoyancy time series. However, it is possible that such features might occur even in horizontally homogeneous convection—a float might track a parcel being continuously cooled at the surface, which then subducts into a plume, leaving the float behind at the surface in the more buoyant fluid that moves in to take the place of the dense downwelling parcel. However, we would expect the horizontal buoyancy gradients to be much reduced when mesoscale eddies are not present and, hence, the skewness in buoyancy derivative to be smaller, as confirmed by the latter part of Fig. 15. Given these uncertainties, we suggest that horizontal buoyancy fronts might be present in the observations of Lavender et al. (2002), but this is not yet conclusive.

4. Conclusions

We have discussed some of the statistics obtained by isobaric floats in numerically generated convecting and nonconvecting eddy fields. Our principal findings are that the isobaric float measurements of b , τ , and vertical velocity are biased. Floats oversample regions of dense downwelling fluid near the surface. A reasonable explanation of these biases is that the floats may tend to congregate in convergent regions, as for horizontally homogeneous convection. In our particular eddy scenario, these downwelling regions are also associated with saltier fluid (higher τ), due to the initial τ anomaly of the dense-core eddies, leading to biases in the τ field, too. Evidence of the bias can easily be spotted in the double peaks in buoyancy and τ PDFs. Hence, in addition to the temporal variability in individual float records, the presence of a double peak in the PDFs might be used as an indicator that the float ensemble has sampled a period of active convection. This would, however, require sufficient float density to sample the mesoscale eddy field and would only serve as an indicator of convection when the mesoscale eddy field is similar to that studied here.

At middepth, the float errors are more complicated since the association of convergence with a density anomaly and tracer anomaly changes with time as the convective layer deepens. When the floats are below the convective layer there is a small downward bias in vertical velocity, with a trend toward denser, higher τ fluid. Once the convective layer penetrates to this depth, an upward bias in vertical velocity, associated with lighter, low τ fluid is seen, reversing the earlier biases in the tracer quantities.

We see that little change appears to be made to the dispersion of the floats when there is convection as compared to a nonconvecting eddy field, and in both cases, for this eddy field, we see normal diffusion. However, convection encourages a more rapid exchange of floats between light and dense eddies. Signals of this exchange—sudden jumps in the tracer values—can be seen in individual float records.

The PALACE floats of Lavender et al. (2002) are stationed at a depth of 400 m and experience an initial upward bias in vertical velocity (like our floats at 1 km) followed by a downward bias at later times. This might be interpreted as a consequence of the deepening mixed layer; the floats are initially at the base of the convective layer but, later in the winter, are in the top half of the convective layer (which deepens to > 1500 m) and hence have a downward vertical velocity bias.

Our simulations of isobaric float responses to convection in the presence of mesoscale eddies show similar sampling biases to simulations of convection without mesoscale eddies (Harcourt 1999; Lherminier et al. 2001). One difference between calculations with and without mesoscale eddies is in the tracer variance measured by the isobaric floats: without mesoscale eddies the isobaric float measurement of tracer variance is less than the Eulerian value, whereas we find with mesoscale eddies that the isobaric float measurement is greater than the Eulerian value. However, the numerical studies without eddies (e.g., Harcourt 1999) did not estimate the variance by removing the sample mean, but rather by high-pass filtering each individual time series. As we have shown, for a scenario in which most of the buoyancy variance is generated by the mesoscale eddy field, this tends to greatly reduce the estimated variance, particularly when the filtering timescale is short. For initially horizontally homogeneous scenarios, we might suppose that the buoyancy varies on the same short timescales as the vertical velocity so that there is little difference between the two different methods of variance estimation. The increase in variance estimated by the isobaric floats in our calculations as compared to the Eulerian value is a consequence of the eddy field in our calculations, which leads to the emergence of a double peak in the isobaric PDF—one

peak corresponding to the eddy distribution of tracer and the other to the tracer distribution in downwelling regions.

We have also shown that, when baroclinic instability associated with the eddy field is dominant, individual float time series are characterized by sudden increases in buoyancy with more gradual decreases. This skewness in the buoyancy time derivative decreases as upright plume convection takes over when horizontal gradients have been eroded.

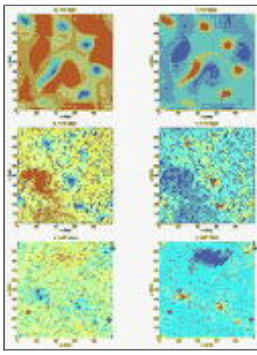
Acknowledgments

We would like to acknowledge helpful discussions with Ramsey Harcourt, Joe Lacasce, and Kara Lavender, and useful suggestions from an anonymous reviewer. Support for this study was provided by ONR Grants N00014-95-1-0316, N00014-98-1-0051, and N00014-98-1-0165. Computations were performed at the San Diego Supercomputer Center. SL was partially supported by the Penzance Endowed Fund in Support of Assistant Scientists administered by the Woods Hole Oceanographic Institution.

References

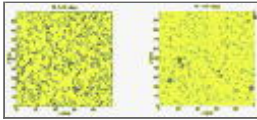
- Chandrasekar S., 1943: Stochastic problems in physics and astronomy. *Rev. Mod. Phys.*, **15**, 1–89. [Find this article online](#)
- D'Asaro E. A., D. M. Farmer, J. T. Osse, and G. T. Dairiki, 1996: A Lagrangian float. *J. Atmos. Oceanic Technol.*, **13**, 1230–1246. [Find this article online](#)
- Harcourt R. R., 1999: Numerical simulation of deep convection and the response of drifters in the Labrador Sea. Ph.D. thesis, University of California, Santa Cruz, 367 pp.
- Harcourt R. R., L. Jiang, and R. W. Garwood, 1997: Numerical simulation of drifter response to Labrador Sea convection. Naval Postgraduate School Tech. Rep. NPS-OC-97-003, 70 pp.
- Harcourt R. R., E. L. Steffen, R. W. Garwood, and E. A. D'Asaro, 2002: Fully Lagrangian floats in Labrador Sea deep convection: Comparison of numerical and experimental results. *J. Phys. Oceanogr.*, **32**, 493–510. [Find this article online](#)
- Lab Sea Group, 1998: The Labrador Sea Deep Convection Experiment. *Bull. Amer. Meteor. Soc.*, **79**, 2033–2058. [Find this article online](#)
- Lavender K. L., R. E. Davis, and W. B. Owens, 2002: Observations of open-ocean deep convection in the Labrador Sea from subsurface floats. *J. Phys. Oceanogr.*, **32**, 511–526. [Find this article online](#)
- Legg S., and J. C. McWilliams, 2000: Temperature and salinity variability in heterogeneous ocean convection. *J. Phys. Oceanogr.*, **30**, 1188–1206. [Find this article online](#)
- Legg S., and J. C. McWilliams, 2001: Convective modifications of a geostrophic eddy field. *J. Phys. Oceanogr.*, **31**, 874–891. [Find this article online](#)
- Legg S., J. C. McWilliams, and J. Gao, 1998: Localization of deep ocean convection by a mesoscale eddy. *J. Phys. Oceanogr.*, **28**, 944–970. [Find this article online](#)
- Lherminier P., R. R. Harcourt, R. W. Garwood, and J.-C. Gascard, 2001: Interpretation of mean vertical velocity measured by isobaric floats during deep convective events. *J. Mar. Syst.*, **29**, 221–237. [Find this article online](#)
- McWilliams J. C., Coauthors, 1983: The local dynamics of eddies in the western North Atlantic. *Eddies in Marine Science*, A. R. Robinson, Ed., Springer-Verlag, 92–113.
- Moeng C.-H., and J. C. Wyngaard, 1988: Spectral analysis of large eddy simulations of the convective boundary layer. *J. Atmos. Sci.*, **45**, 3575–3587. [Find this article online](#)
- Taylor G. I., 1921: Diffusion by continuous movements. *Proc. London Math. Soc.*, **20**, 196–212. [Find this article online](#)

Figures



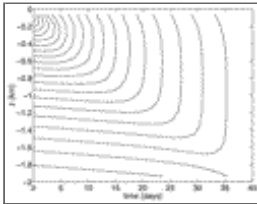
[Click on thumbnail for full-sized image.](#)

FIG. 1. Snapshots of the near-surface buoyancy and τ fields at the start of the calculation, and on the 12th and 37th days of cooling. Superimposed are crosses marking the location of the floats. Large colored crosses mark the locations of the four individual floats discussed in the text. Reds and yellows represent high values, blues and greens low values. The color scale changes with time, in order to accommodate the changing mean buoyancy and τ , with values $24.9 < b < 80.5 \times 10^{-5} \text{ m s}^{-2}$, $-145.2 < \tau < -89.6 \times 10^{-5} \text{ m s}^{-2}$ initially and $-1.2 < b < 12.7 \times 10^{-5} \text{ m s}^{-2}$, $-82.6 < \tau < -52.92 \times 10^{-5} \text{ m s}^{-2}$ at $t = 37$ days



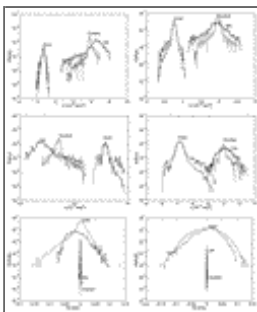
[Click on thumbnail for full-sized image.](#)

FIG. 2. Snapshots of the vertical velocity at $z = -62.5 \text{ m}$ on the 12th and 37th days of cooling. Superimposed are crosses marking the location of the floats. Large colored crosses mark the location of the four individual floats discussed in the text. Reds represent high values, blues and greens low values, and yellows show values close to zero. The vertical velocity takes values between $-0.20 \rightarrow 0.13 \text{ m s}^{-1}$



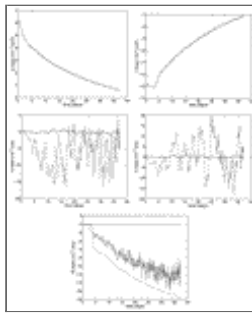
[Click on thumbnail for full-sized image.](#)

FIG. 3. The horizontally averaged Eulerian measurement of buoyancy b shown as a function of depth and time. The contour spacing is $3 \times 10^{-5} \text{ m s}^{-2}$. The depth of the convectively modified region can be deduced from the extent of the modifications to the original isopycnal structure



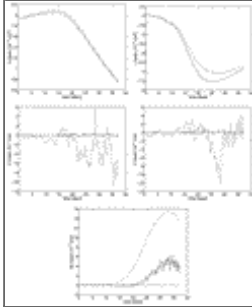
[Click on thumbnail for full-sized image.](#)

FIG. 4. Probability density functions of buoyancy b , spice τ , and vertical velocity W (left) near the surface and (right) at middepths. Each plot shows the PDFs from the initial conditions (Init) from both the floats (dashed) and the Eulerian grid (solid), the PDFs 37 days later with surface forcing (Cool) from both floats (dashed) and the Eulerian grid (solid), and the PDFs 37 days later without surface forcing (Control) from both floats (dotted) and the Eulerian grid (solid). Initially, the floats are regularly spaced (Init), but at the end of Cool and Control the floats have migrated with the flow and are no longer on a regular grid



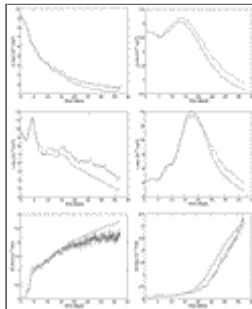
[Click on thumbnail for full-sized image.](#)

FIG. 5. Time series of the Eulerian mean (solid) and isobaric float mean (dashed) near the top surface for buoyancy b , spice τ , zonal velocity U , meridional velocity V , and vertical velocity W . Also shown on the W plot is γW_{rms} (dotted), where γ is the (Eulerian) correlation between the vertical velocity and convergence dW/dz at this level, $\gamma = \langle W dW/dz \rangle / (W_{\text{rms}} dW/dz_{\text{rms}})$, and W_{rms} is the Eulerian rms vertical velocity



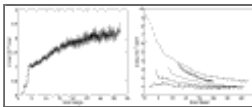
[Click on thumbnail for full-sized image.](#)

FIG. 6. Time series of the Eulerian mean (solid) and isobaric float mean (dashed) at middepths for b , τ , U , V , W . Also shown on the W plot is γW_{rms} , where γ is the (Eulerian) correlation between the vertical velocity and convergence dW/dz at this level, $\gamma = \langle W dW/dz \rangle / (W_{\text{rms}} dW/dz_{\text{rms}})$, and W_{rms} is the Eulerian rms vertical velocity



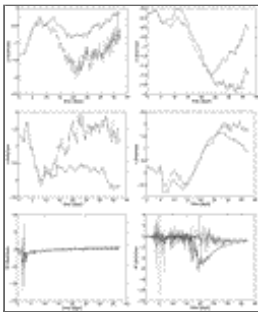
[Click on thumbnail for full-sized image.](#)

FIG. 7. Time series of the Eulerian rms (solid) and isobaric float rms (dashed) for b , τ , and W (left) near the surface and (right) at middepth



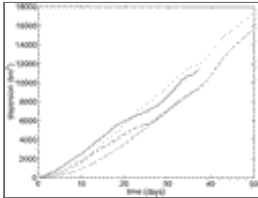
[Click on thumbnail for full-sized image.](#)

FIG. 8. The rms variation in vertical velocity W and buoyancy b , estimated from near-surface floats on time periods less than 3.3 days (dotted), 8.2 days (solid), (buoyancy only) 16.4 days (dot-dashed), and 24.6 days (thick solid). Also shown is the isobaric ensemble average estimate of the rms, as shown previously (dashed). Here the high-frequency component of each time series W'_i and b'_i is obtained by removing the temporal running mean obtained by summing over the averaging window. The variance W'^2 , b'^2 is then summed over all floats.



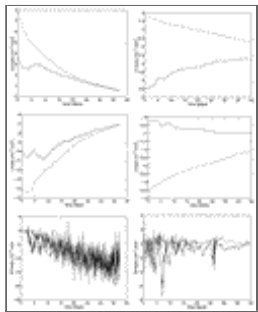
[Click on thumbnail for full-sized image.](#)

FIG. 9. Time series of the Eulerian skewness (solid) and isobaric float skewness (dashed) for b , τ , and W (left) near the surface and (right) at middepth



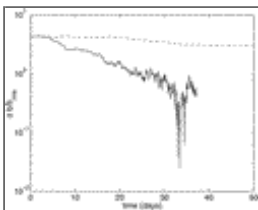
[Click on thumbnail for full-sized image.](#)

FIG. 10. Time series of the float dispersion both with and without surface cooling: with cooling, near surface (solid); with cooling, at middepths (dashed); without cooling, near surface (dotted); without cooling, at middepths (dot-dashed)



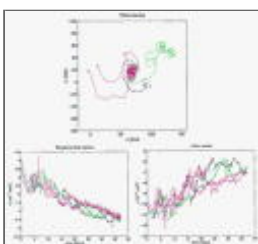
[Click on thumbnail for full-sized image.](#)

FIG. 11. The mean buoyancy b , spice τ , and vertical velocity W in the surface layer, measured by floats initially in dense eddies (solid) and initially in light eddies (dashed), both (left) with and (right) without convection



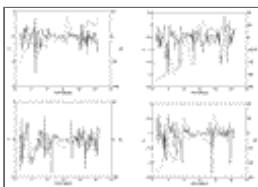
[Click on thumbnail for full-sized image.](#)

FIG. 12. The difference in ensemble mean buoyancy between floats initially in light eddies and floats initially in dense eddies (Δb) scaled by the Eulerian buoyancy rms, as a function of time for both the cooled scenario (solid line) and the control case (dashed line)



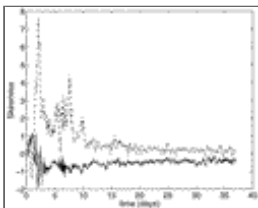
[Click on thumbnail for full-sized image.](#)

FIG. 13. (top) The tracks of four individual floats, all initially in or near the same dense eddy. (bottom) The buoyancy and the spice signal recorded by these floats



[Click on thumbnail for full-sized image.](#)

FIG. 14. Time series showing the vertical velocity (solid) and buoyancy anomaly (dashed) for the individual floats shown in [Fig. 13](#), during the time period over which mesoscale eddy instability dominates the convective mixing



[Click on thumbnail for full-sized image.](#)

FIG. 15. The skewness of the time derivative of buoyancy (dashed) and vertical velocity (solid) measured by the near-surface isobaric floats

* Woods Hole Oceanographic Institution Contribution Number 10248.

Corresponding author address: Dr. Sonya Legg, Woods Hole Oceanographic Institution, Woods Hole, MA 02543. E-mail: slegg@whoi.edu

[top ▲](#)



© 2008 American Meteorological Society [Privacy Policy and Disclaimer](#)

Headquarters: 45 Beacon Street Boston, MA 02108-3693

DC Office: 1120 G Street, NW, Suite 800 Washington DC, 20005-3826

amsinfo@ametsoc.org Phone: 617-227-2425 Fax: 617-742-8718

[Allen Press, Inc.](#) assists in the online publication of AMS journals.